Supplemental Figure 1. Transfection with Halotag-fused HTT *exon 1* (Q18) and mHTT *exon 1 (Q46)* constructs with and without the PRD. Representative photomicrographs of primary cortical neurons expressing HTT *exon 1* (Q18) or mHTT *exon 1* (Q46) with and without the PRD (ΔPRD). At 4 DIV, cortical neurons were transfected with the following Halotag-fused protein constructs: **A)** HTT exon 1 (Q18), **B)** HTT *exon 1* (Q18 ΔPRD), **C)** mHTT *exon 1* (Q46), and **D)** mHTT *exon 1* (Q46 ΔPRD). At 6DIV, cells were incubated overnight with the halotag TMR ligand (red). At 7 DIV, cells were fixed and processed for immunolabeling with βIII tubulin (green). Transfection with mHTT *exon 1* constructs containing Q18, Q18 ΔPRD or Q46 ΔPRD have little or no effect on neuronal viability, but transfection with mHTT *exon 1* constructs containing Q46 with an intact PRD leads to degeneration of transfected cells. Scale bars=20μm.

Supplemental Figure 2. The fluorescent, neuron-specific, transient membrane-permeant label, NeuO, displayed no toxic effects on axonal outgrowth over time. To verify that neurons remained viable and continued growing in the microfluidic chambers, we performed live imaging of axons elongating within the microchannels of our custom microfluidic chambers. The same neurons were repeatedly visualized with the live neuronal marker, NeuO, at 6 (**A**), 8 (**B**), 11 (**C**), and 13 (**D**) days *in vitro* (DIV). The axon length within each microchannel was measured as it entered the microchannel from the somatodendritic compartment (SDC) until it reached the axon terminal compartment (ATC). Scale bar = 50μm. E) The total number of axons elongating and degenerating in NeuO-treated cortical neurons (N = 261) was quantified over time (see **Fig 4E**).

Supplemental Figure 3. Representative photomicrographs of primary cortical neuron axons within the axon terminal compartment of microfluidic chambers. Live imaging of axons elongating within the axon terminal compartment (ATC) were visualized with the live neuronal marker, NeuO, at 13 DIV, following transfection at 6 DIV with either mHTT *exon 1* (Q46) (**A, B**) or mHTT *exon 1* (Q46 ΔPRD) (**C, D)**. Note the dramatically reduced number of axons reaching the ATC for neurons transfected with mHTT *exon 1* (Q46), compared to neurons transfected with mHTT *exon 1* (Q46 ΔPRD). Scale bars=50μm.

Supplemental Figure 4. Increased PRD exposure in striatal tissue of zQ175 mice, compared to wild type mice. A) A full-length HTT schematics shows the approximate location of antibody (Ab) epitopes used for quantitative immunoblots in **B-D. B)** TX-100 1%-soluble proteins were extracted under native conditions from striata of WT and zQ175 mice (n=6 mice/genotype; 12 samples total). Two microliter aliquots (containing approximately 4µg protein each) from each sample were spotted in triplicate on nitrocellulose membranes and analyzed by quantitative immunoblotting as described in Materials and Methods. Compared to samples prepared from wild type mice, samples prepared from zQ175 displayed reduced levels of D7F7 Ab immunoreactivity (rabbit monoclonal, in green). In contrast an Ab recognizing synaptophysin (synaptoph; mouse monoclonal, in red) showed similar immunoreactivity levels among all samples. Quantitative LI-COR-based analysis of D7F7/synaptophysin immunoreactivity ratios confirmed these observations (see **Fig 5A**), suggesting reduced levels of total TX-100-soluble HTT protein in zQ175 mice, compared to WT mice. These results also supported findings of decreased D7F7 immunoreactivity using immunohistochemistry approaches (see **Fig. 5C**). **C-D)** Same samples as in B were spotted on the membranes shown in Panels C and D and analyzed first by quantitative immunoblotting using anti-D7F7 Ab (rabbit monoclonal, in green), which was used for total HTT normalization. **C)** The membrane shown in this panel was re-blotted with MW7 (mouse monoclonal IgM), an Ab recognizing polyP stretches within the PRD in HTT. Quantitative LI-COR-based analysis showed increased D7F7/MW7 immunoreactivity ratios in striatal samples prepared from zQ175 mice, compared to wild type mice (see plot on the right). **D)** The membrane shown in this panel was re-blotted with 4C9, a mouse monoclonal IgG Ab that recognizes amino acids 51-71 within the PRD in HTT. Quantitative LI-COR-based analysis showed increased D7F7/MW7 immunoreactivity ratios in striatal samples prepared from zQ175 mice, compared to wild type mice (see **Fig 5**). Collectively, these results supported increased exposure of the PRD in mHTT, compared to WT-HTT.

Supplemental Figure 5. Increased PRD exposure and JNK activation in the striatal tissues of HD patients at various stages. Consistent with findings in **Fig 6,** enhanced resolution Structured Illumination Microscopy revealed increased MW7 immunoreactivity and JNK activation in striatal tracts and nuclei of tissue from HD patients. The difference was clear in the Grade 1 HD striatum, where both nuclei and

axonal tracts were better preserved, as indicated by Hoechst and Tubb3 staining respectively, compared with Grade 2 and 3 HD cases. However, local accumulation of MW7 and phosphorylated JNK were more prominent in the nuclei, together with neuronal loss and disruption in microtubule organization in axonal tracts, especially at the later stage (i.e., HD-3). It is worth noting that there was a noticeable level of heterogeneity in these HD patient tissues, at least partially due to both physiological heterogeneity in the striatum and pathological heterogeneity in the disease. Therefore, further studies are required and are currently underway.

Supplemental Figure 6. A synthetic peptide encompassing the P1 PRD subregion suffices to inhibit fast axonal transport in isolated axoplasm by activation of JNK kinases. A) To verify that the peptide sequences in the PRD were sufficient activate JNK kinases and inhibit fast axonal transport, a synthetic peptide corresponding to the P1 sequence (see **Fig. 5A**) was generated. **B)** Plot depicting the effects of this peptide on fast axonal transport. The P1 synthetic peptide had an effect on fast axonal transport comparable to mHTT exon 1 (Q49) (see **Fig. 2A**) or the GST-P1 fusion protein (**Fig. 5B**), inhibiting both directions of fast axonal transport. **C)** As observed with GST-P1 (**Fig 7E**), effects of the P1 synthetic peptide on fast axonal transport were also blocked by addition of the selective JNK inhibitor SP600125

Supplemental Figure 7. GST-PRD activates JNK kinases in isolated axoplasm. A) Representative immunoblots of "sister" axoplasms extruded from six squid. For each squid, one axoplasm was perfused with control buffer (Buffer X/2; CTRL), and its corresponding sister axoplasm was perfused with Buffer X/2 plus 2μM GST-PRD as described previously[21]. After 50 minutes incubation, axoplasms were homogenized, lysates separated by SDS-PAGE, and analyzed by quantitative LI-COR based immunoblotting using antibodies against phosphorylated (active) JNK (pJNK). Immunoblotting of membranes with anti- kinesin heavy chain antibodies (KHC) provided a loading control. **B)** Quantitative data shows increased JNK activation in axoplasms perfused with GST-PRD, compared to sister axoplasms perfused with control buffer (n = 6). Levels of pJNK immunoreactivity were normalized to KHC immunoreactivity to correct for protein loads. Changes in activity were assessed by comparing normalized pJNK activity with GST-PRD perfusion to buffer X/2 perfusion

(Vehicle) for each squid. Immunoreactivity for pJNK was increased by an average of 21%, which was significant at p = 0.0072 in a paired t-test of (μ1-μ2) using Data Desk 8.3 statistical software.

Supplemental Figure 8. Crystal structure of HTT *Exon 1*. X-ray crystal structure of human HTT *exon 1* (Q17) using data for structure 310W HTTp://www.rcsb.org/3d-view/3IOW[59] suggests a possible mechanism to explain why expansion of the polyQ motif leads to pathogenicity. The protein was visualized in Cn3D 4.3 software from NCBI. The polyQ domain is not defined in this view but is normally on top of the PRD[59]. In this image, P1 peptide sequence of the PRD is exposed on the surface of HTT *exon 1* (P1, in yellow). The polyQ is not well defined in this structure, but several lines of evidence suggest that expansion of the polyQ sequence to >36Q increases exposure of the PRD[24,34,59]. PolyQ expansion may destabilize the polyQ-PRD interaction, aberrantly exposing P1. Increased P1 (and possibly P3) exposure would facilitate an interaction with one or more SH3 domain-containing downstream protein effector(s).

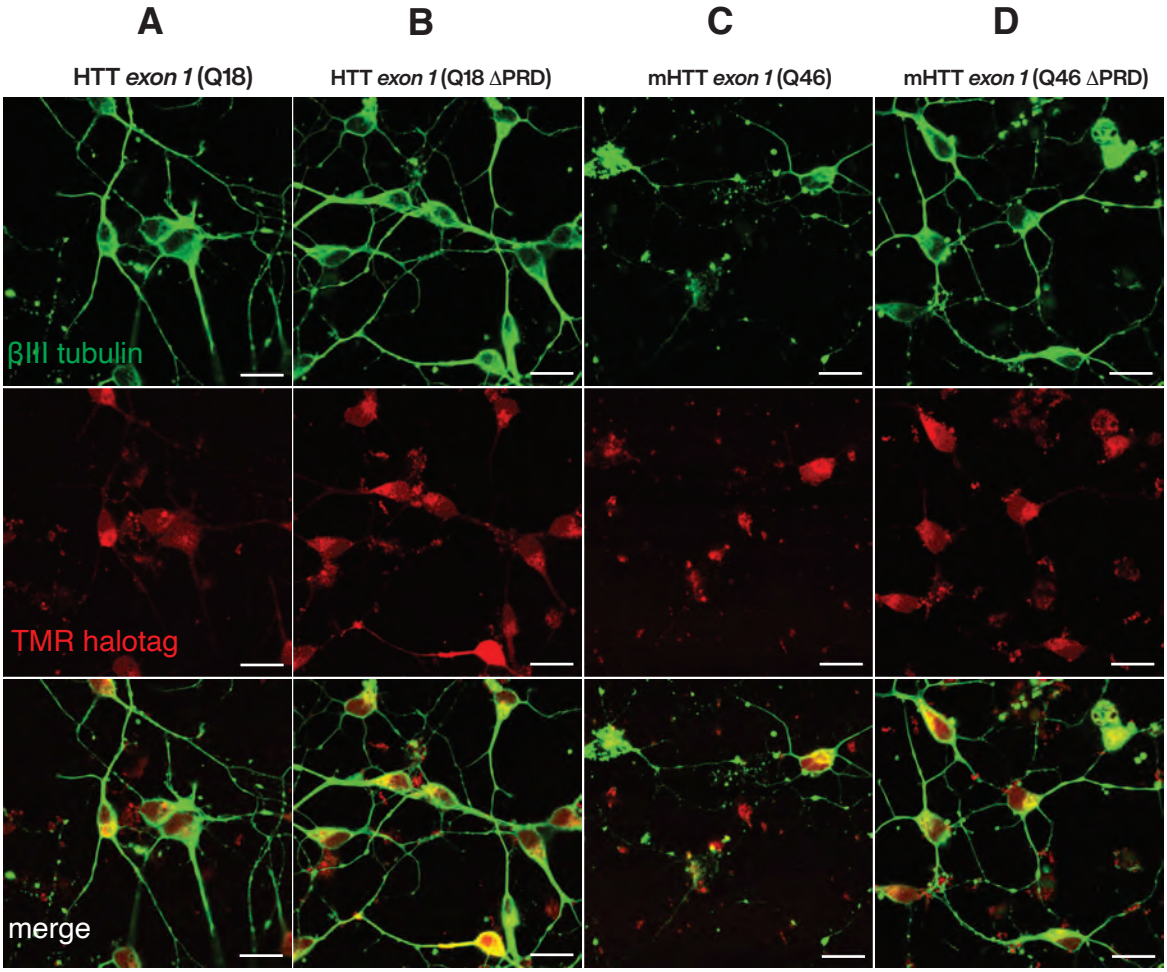

Supplementary Figure 1

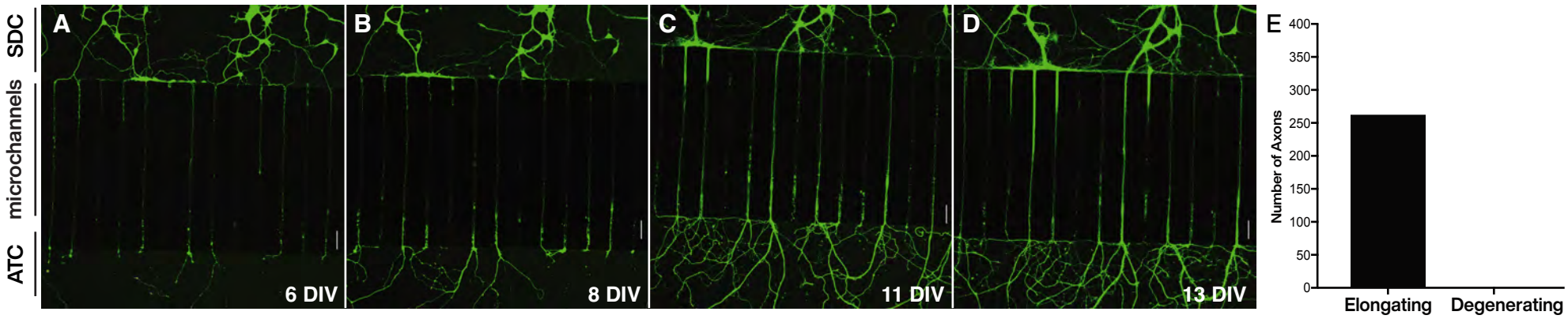

Supplementary Figure 2

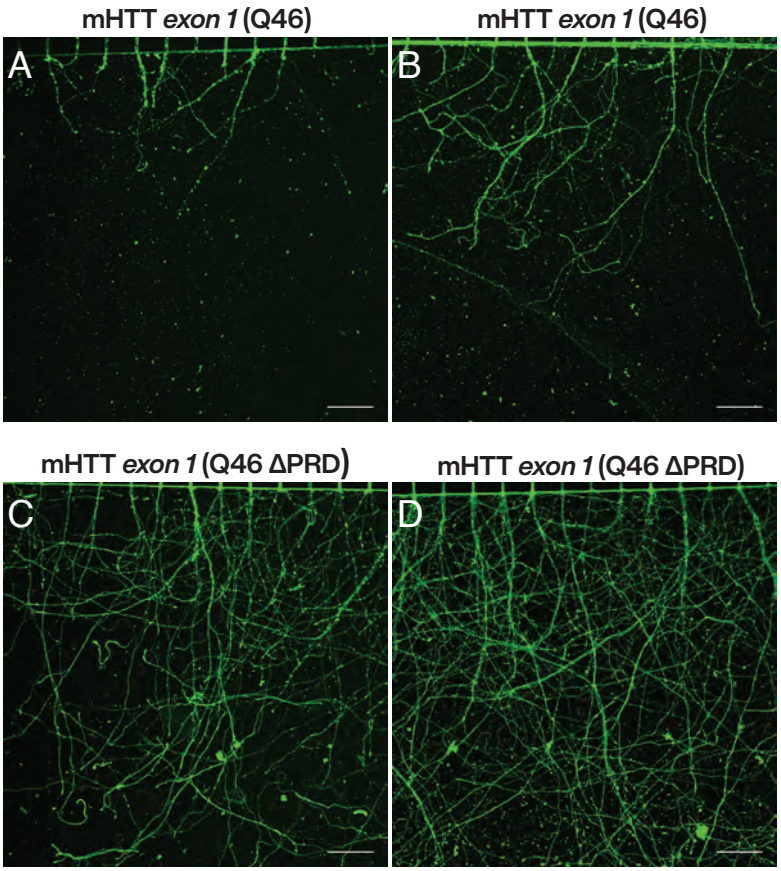

Supplementary Figure 3

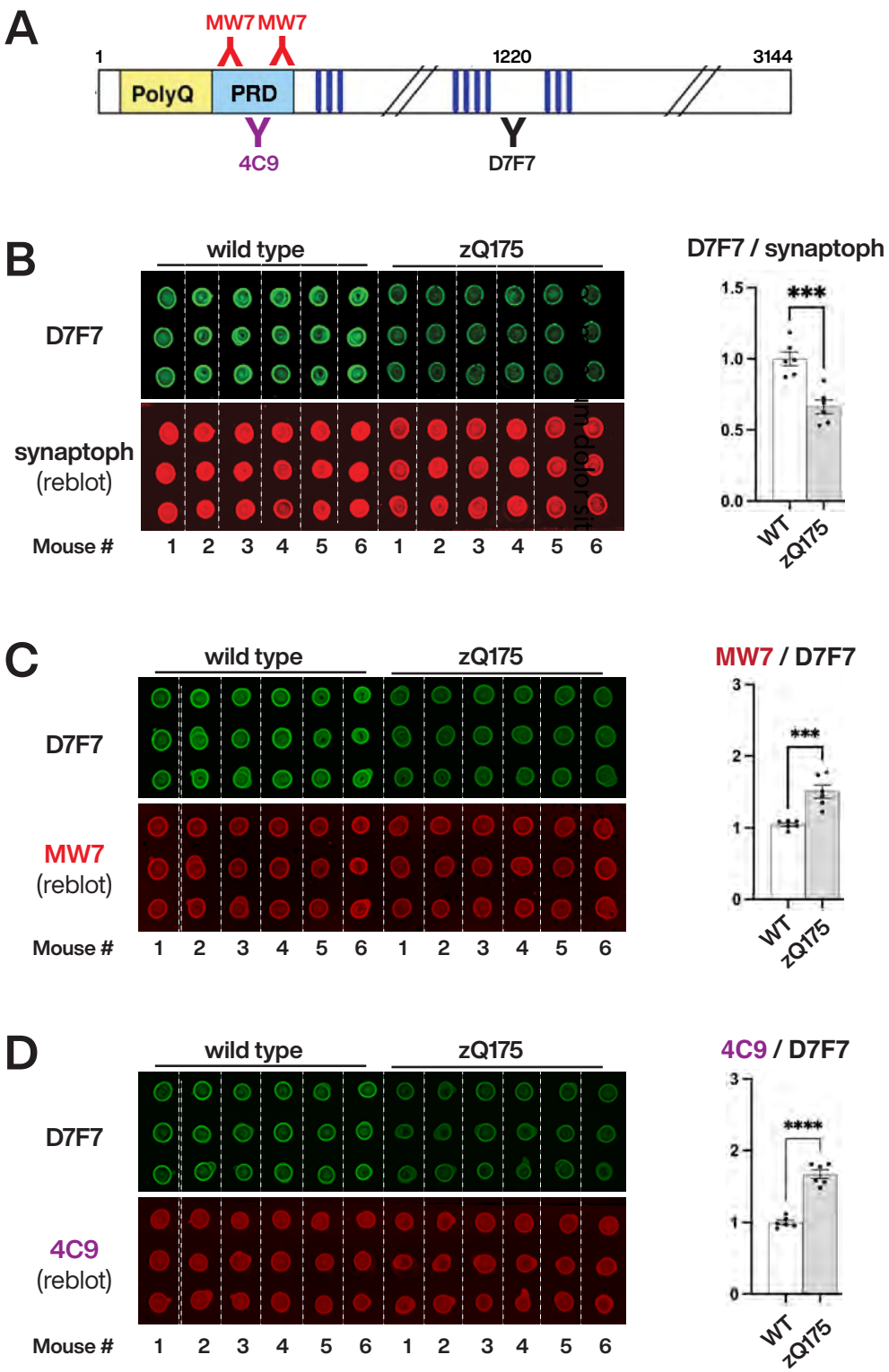

Supplementary Fig. 4

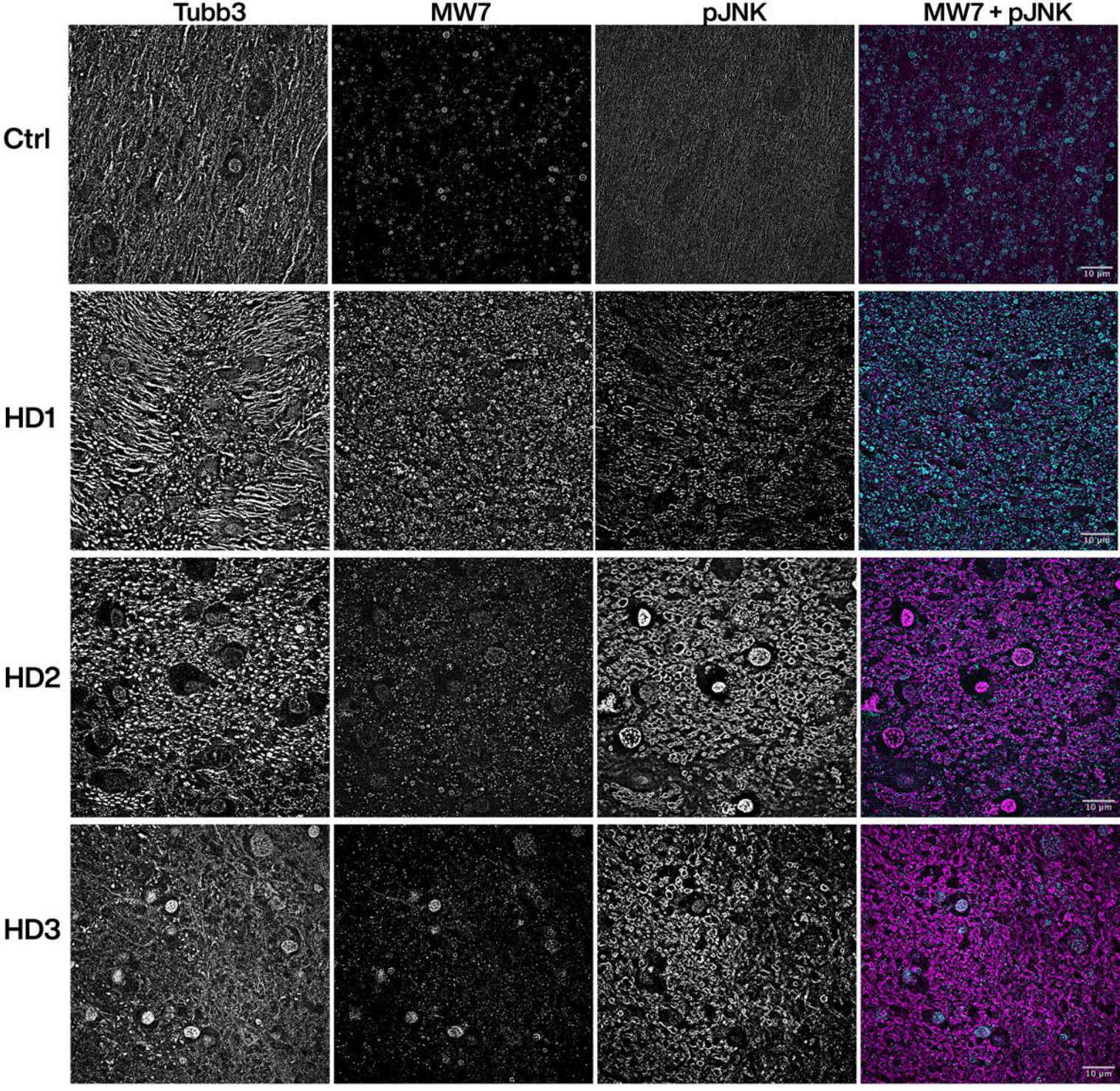

Supplementary Fig. 5

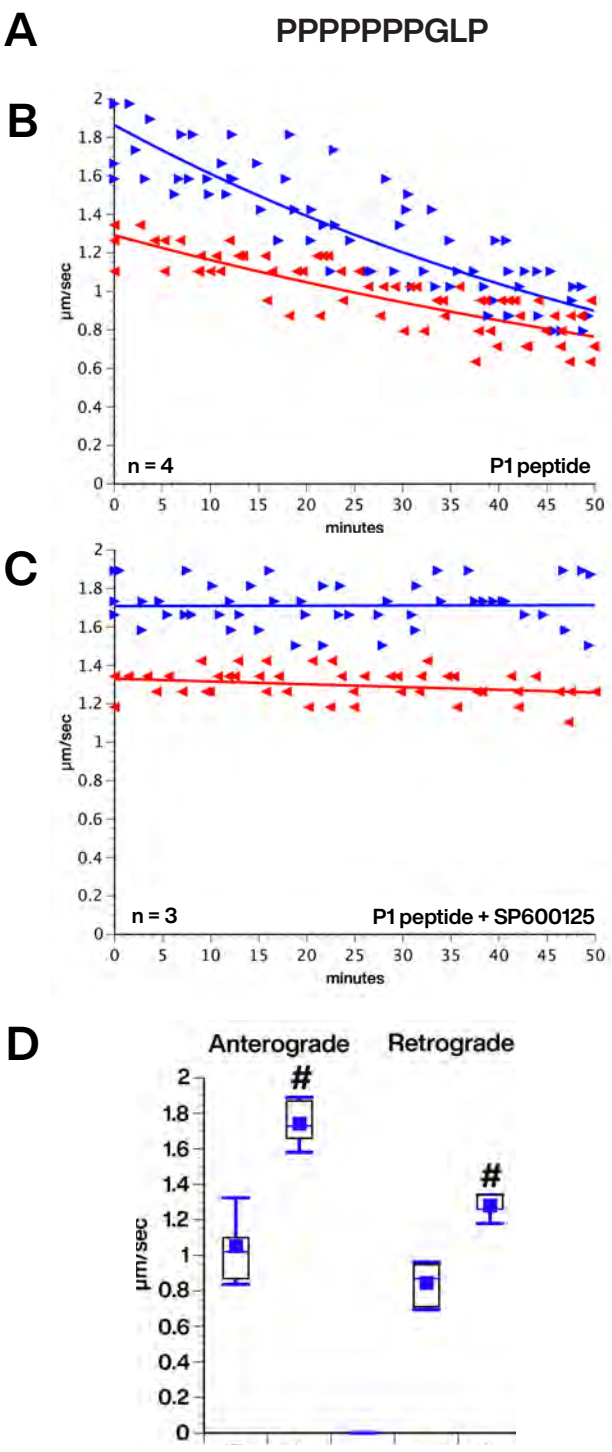

Supplementary Figure 6

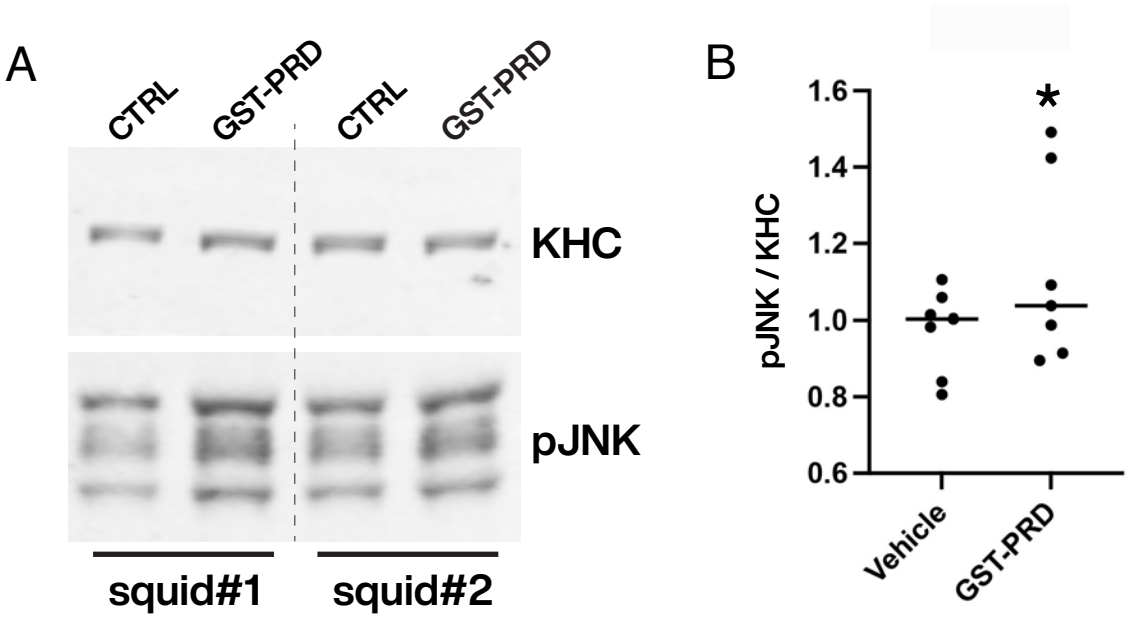

Supplementary Figure 7

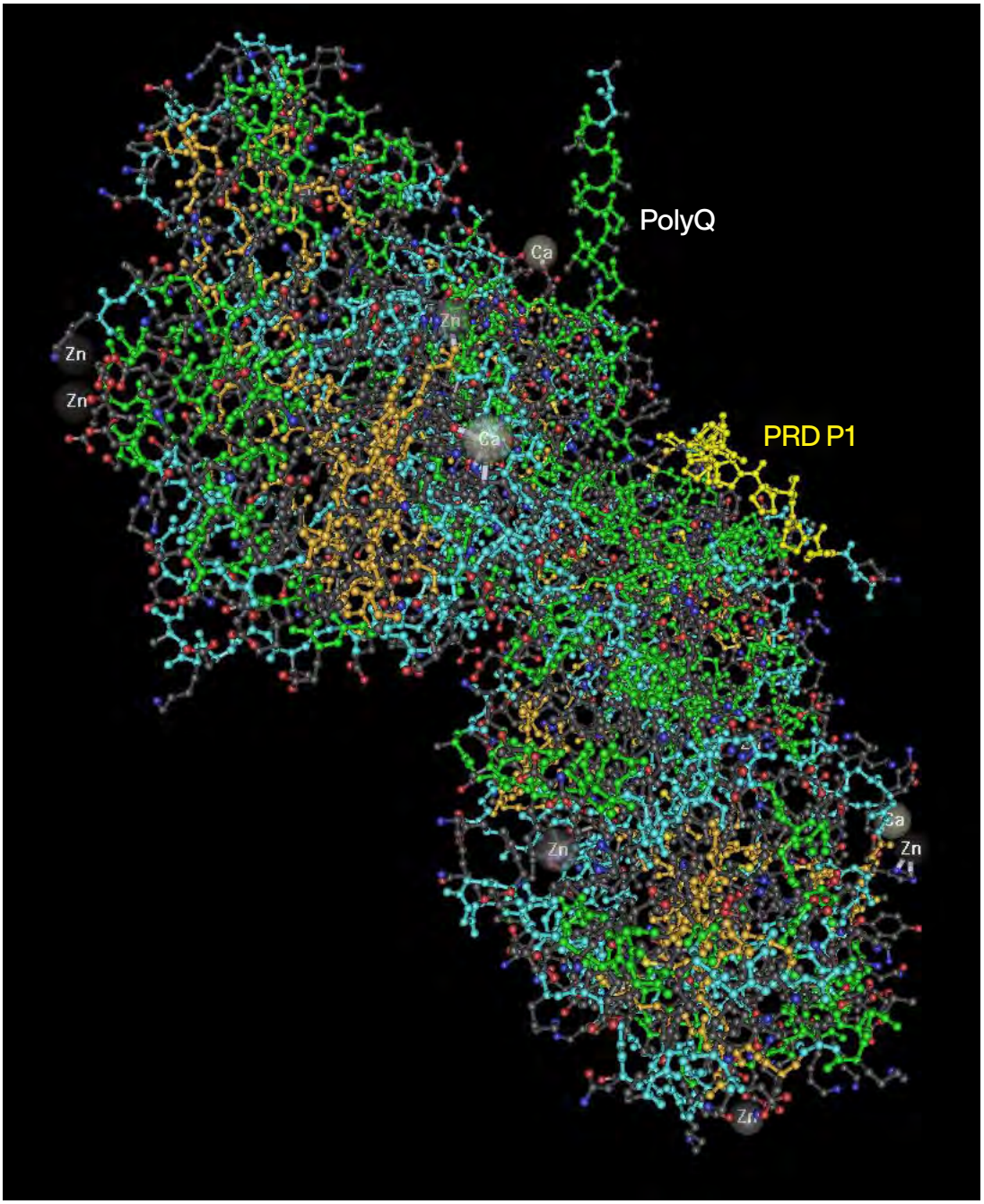

Supplemental Figure 8

SUPPLEMENTARY TABLE 1: ANTIBODIES USED IN THIS STUDY

Primary antibodies				
Antibody Name	**Target protein/Epitope**	**Species**	**Source / reference**	**experiments in Fig(s).**
MW1	HTT (polyglutamine tract)	mouse monoclonal IgG	Developmental Studies Hybridoma Bank. [1]	Fig. 1D
MW7	HTT. Polyproline stretches within P1 and P3 subregions of the PRD.	mouse monoclonal IgM	Developmental Studies Hybridoma Bank. [1]	Fig. 1E Fig. 5 Fig. 6 Suppl. Fig 8
2B7	HTT (aa 7-13)	mouse monoclonal IgG	CHDI Foundation Coriell Inst. Med CH00705. [2]	Suppl. Fig. 4
4C9	HTT aa 51-71 (PRD region)	mouse monoclonal IgG	CHDI Foundation Coriell Inst. Med CH00708. [2]	Suppl. Fig. 4
D7F7	HTT. Residues surrounding P1218 of human HTT.	rabbit monoclonal	Cell Signalling Technology mAb#5656 (lot#6) [3]	Fig. 5 Fig. 6 Suppl. Fig. 4
Anti-Phosphorylated SAPK/JNK (Thr183/Tyr185)	JNK kinases. Residues surrounding Thr183/Tyr185 of human JNK.	rabbit monoclonal (clone 81E11)	Cell Signaling Technology #4668 (lot#24).	Fig. 5 Fig. 6 Suppl. Fig 8
Anti-Total JNK	JNK kinases. Epitope mapping between Ser2-and Ile384 of human JNK	mouse monoclonal IgG2A (clone 252355)	R&D Systems#MAB1387 (lot# KQT0216082).	Fig. 5
Anti-Synaptophysin:	Synaptophysin.	mouse monoclonal IgG1 (clone SVP38)	Santa Cruz Biotechnologies #12737.	Fig. 5 Suppl. Fig. 4
Anti-DARPP-32	DARPP-32. Residues surrounding Glu160 of human DARPP-32.	rabbit monoclonal (clone 19A3)	Cell Signaling Technology #2306.	Fig. 5
Alexa Fluor® 488 Anti-beta III Tubulin	Neuronal betaIII tubulin.	Mouse Monoclonal [2G10]	Abcam, ab195879	Fig. 6 Suppl. Fig 8
Secondary antibodies used in westerns and dot blots.				
Antibody Name	**Conjugated dye**	**Species**	**Source / reference**	**experiments in Fig(s).**
anti-rabbit IgG	IRDye 800CW	Goat serum	LI-COR #926-32211 (lot# C70620-05)	Fig. 5 Fig.6 Suppl. Fig. 4
anti-rabbit IgG	IRDye 680CW	Goat serum	LI-COR #926-68071 (lot D11012-15)	Fig. 5 Suppl. Fig. 4
anti-mouse IgG	IRDye 800CW	Goat serum	LI-COR#926-32210, (lot#D10825-15)	Fig. 5 Suppl. Fig. 4
anti-mouse IgG	IRDye 680CW	Goat serum	LI-COR#925-68070 (lot#C10217-05)	Fig. 5 Suppl. Fig. 4
anti-mouse IgM	IRDye 680RD	Goat serum	LI-COR#925-68180 (lot# D20708-04)	Fig. 5 Fig. 6 Suppl. Fig. 4
Secondary antibodies used for Immunohistochemistry.				
Antibody Name	**Conjugated dye**	**Species**	**Source / reference**	**experiments in Fig(s).**

anti-rabbit IgG	Alexa fluor 568	Goat serum	Invitrogen#A11011 (lot#: 2277758)	Fig. 5
anti-Mouse IgM, µ chain specific	Alexa fluor 594	Goat serum	Jackson Immuno Research # 115-585-075 (lot#: 148758)	Fig. 5
anti-Mouse IgM, µ chain specific	Alexa fluor 568	Goat serum	Abcam ab175702	Fig. 6 Suppl. Fig 8
Anti-Rabbit IgG, highly crossed-adsorbed	CF647	Goat serum	Biotium 20282	Fig. 6 Suppl. Fig 8
Immunohistochemistry-related reagents.				
Name			**Source / reference**	**experiments in Fig(s).**
DAPI			Sigma-Aldrich #D9542 (lot#079M4003V)	Fig. 5
Hoechst			ThermoFisher H1399	Fig. 6

REFERENCES

1. Ko, J., S. Ou, and P.H. Patterson, New anti-huntingtin monoclonal antibodies: implications for huntingtin conformation and its binding proteins. Brain Res Bull, 2001. 56(3-4): p. 319-29.
2. Weiss, A., et al., Single-step detection of mutant huntingtin in animal and human tissues: a bioassay for Huntington's disease. Anal Biochem, 2009. 395(1): p. 8-15.
3. Smith, E.J., et al., Early detection of exon 1 huntingtin aggregation in zQ175 brains by molecular and histological approaches. Brain Commun, 2023. 5(1): p. fcad010.

Supplementary Table 2: Case Information for dot blot experiments in Figure 6

ID	Age	Sex	NPDX1	NPDX2	NPDX3	PMI	HD_Grade
Ctrl1	63	Male	CVD	AH	ADNC	18	N/A
Ctrl2	73	Male	CVD	AH	ADNC	14	N/A
Ctrl3	59	Male	Tauopathy	CVD		35	N/A
HD1	51	Male	HD			23	HD_2
HD2	71	Male	HD			24	HD_1
HD3	70	Male	HD	INF		52	HD_2

CVD: Cerebrovascular Disease

AP: Acute Hypoxia

ADNC: Alzheimer's Disease Neuropathological Change

INF: Infarcts

Supplementary Table 3: Case Information for IHC experiments in Figure 6

ID	Age	Sex	NPDX1	NPDX2	NPDX3	PMI	HD_Grade
Ctrl_A	56	Male	Control			36	N/A
Ctrl_B	60	Male	Control			14	N/A
Ctrl_C	56	Female	Control	Acute Hypoxia	Cerebrovascular Disease (CVD)	8	N/A
Ctrl_D	68	Female	Control	Cerebrovascular Disease (CVD)		20	N/A
Ctrl_E	73	Male	Control	Cerebrovascular Disease (CVD)	Acute Hypoxia	14	N/A
HD_A	48	Female	Huntington's Disease Grade 1 (HD-1)			12	HD-1
HD_B	69	Male	Huntington's Disease Grade 1 (HD-1)			9	HD-1
HD_C	71	Male	Huntington's Disease Grade 1 (HD-1)			24	HD-1
HD_D	53	Female	Huntington's Disease Grade 2 (HD-2)	Cerebrovascular Disease (CVD)		16	HD-2
HD_E	73	Male	Huntington's Disease Grade 2 (HD-2)	Arteriolosclerosis	Acute Hypoxia	24	HD-2
HD_F	51	Male	Huntington's Disease Grade 2 (HD-2)			23	HD-2
HD_G	55	Male	Huntington's Disease Grade 2 (HD-2)	Cerebrovascular Disease (CVD)		16	HD-2
HD_H	63	Female	Huntington's Disease Grade 3 (HD-3)	Cerebrovascular Disease (CVD)		20	HD-3
HD_I	55	Male	Huntington's Disease Grade 3 (HD-3)	Cerebrovascular Disease (CVD)		7	HD-3
HD_J	74	Female	Huntington's Disease Grade 3 (HD-3)	Cerebrovascular Disease (CVD)		20	HD-3
HD_K	67	Male	Huntington's Disease Grade 3 (HD-3)	Arteriolosclerosis		24	HD-3